Quantum Number Constraints from Shell Structure Govern Short-range Nucleon Pairing

```
D. Nguyen<sup>1,6†</sup>, C. Yero<sup>2,7†</sup>, H. Szumila-Vance<sup>1,8</sup>, F. Hauenstein<sup>1</sup>, N. Swan<sup>2</sup>,
L.B. Weinstein<sup>2*</sup>, J. Kahlbow<sup>4,5</sup>, G.A. Miller<sup>9</sup>, A. Schmidt<sup>3</sup>, E. Piasetzky<sup>4</sup>, O. Hen<sup>5</sup>,
C. Ayerbe Gayoso<sup>9</sup>, E. Cohen<sup>4,14</sup>, P. Datta<sup>10</sup>, A. Denniston<sup>5</sup>, B.R. Devkota<sup>11</sup>,
M. Diefenthaler<sup>1</sup>, C. Fogler<sup>2</sup>, B.R. Gamage<sup>1</sup>, D. Higinbotham<sup>1</sup>, I. Korover<sup>4</sup>,
C. Morean<sup>1</sup>, M. Nycz<sup>12</sup>, M. Satnik<sup>9</sup>, S. Seeds<sup>10</sup> P. Sharp<sup>3</sup>, M. Suresh<sup>13</sup>,
A.S. Tadepalli<sup>1</sup>, R. Wagner<sup>4</sup>, E. W. Wertz<sup>9</sup>

<sup>1</sup>Thomas Jefferson National Accelerator Facility, Newport News, Virginia 23606, USA

<sup>2</sup>Old Dominion University, Norfolk, Virginia 23529, USA
```

³The George Washington University, Washington DC 20052, USA

⁴School of Physics and Astronomy, Tel Aviv University, Tel Aviv 69978, Israel

⁵Massachusetts Institute of Technology, Cambridge, Massachusetts 02139, USA

⁶University of Tennessee, Knoxville, TN 37919, USA

⁷The Catholic University of America, Washington, DC 20064, USA

⁸Florida International University, Miami, FL 33199, USA

⁹University of Washington, Seattle, WA 98195, USA

⁹The College of William & Mary, Williamsburg, Virginia 23185, USA

¹⁰University of Connecticut, Storrs, Connecticut 06269, USA

¹¹Mississippi State University, Mississippi State, Mississippi 39762, USA

¹²University of Virginia, Charlottesville, Virginia 22903, USA

¹³Hampton University, Hampton, Virginia 23669, USA

¹⁴Nuclear Research Center, Negev, Beer-Sheva, Israel 84190

*Corresponding author. Email: weinstein@odu.edu

[†]These authors contributed equally to this work.

Inside atomic nuclei, protons and neutrons can form short-range correlated (SRC) pairs—fleeting, high-momentum interactions that dominate the short-distance structure of nuclear matter. We used high-energy electron scattering to probe SRC pairs in ⁴⁰Ca, ⁴⁸Ca, and ⁵⁴Fe. Surprisingly, we found that SRC pairing depends far more on specific proton and neutron orbitals than on nuclear mass or neutron excess. Our result points to new angular-momentum quantum selection rules governing SRC pairing. This reveals a deep connection between long-range nuclear structure and short-range interactions, relevant to dense nuclear matter such as that found in neutron stars.

While atomic nuclei are complex many-body systems, they are often approximated as nucleons (protons and neutrons) moving independently within shell-model orbitals generated by a mean-field potential. Yet, the complex nature of the nucleon-nucleon force leads to the formation of temporary correlated states that go beyond the mean-field description, including short-range correlated (SRC) pairs (I): tightly-bound, predominantly proton-neutron pairs with high relative momentum and large local density. These pairs dominate the high-momentum tail of the nuclear momentum distribution and account for much of the nucleons' kinetic energy (I–9).

Understanding SRC pair formation is crucial for describing the short-range structure of nuclei and for modeling systems with densities exceeding nuclear saturation, such as neutron stars (10, 11). While SRC pairs have been studied across a range of nuclei, the specific mechanisms driving their formation remain uncertain.

Here we measured the electron-induced knockout of high initial-momentum protons from 40 Ca, 48 Ca, and 54 Fe, see Fig. 1. 40 Ca and 48 Ca are both doubly magic (closed shell), with the latter containing eight (40%) more neutrons in the $1f_{7/2}$ orbital. 54 Fe adds six more protons to the $1f_{7/2}$

orbital, resulting in an almost symmetric, almost doubly-magic nucleus, much like ⁴⁰Ca, but 35% heavier. Therefore by comparing the asymmetric ⁴⁸Ca to the lighter ⁴⁰Ca and the heavier ⁵⁴Fe, we can better understand the roles of the different possible pair-formation mechanisms.

Surprisingly, we find almost no enhancement in the number of protons knocked out from SRC pairs in 48 Ca. However, the additional six $1f_{7/2}$ protons of 54 Fe, lead to $\sim 50\%$ more protons in SRC pairs. These results challenge the expectation that SRC pair formation scales simply with either mass or neutron excess (4). Instead, they suggest that nucleons preferentially form SRC pairs with partners occupying the same orbital, where spatial overlap and angular momentum alignment are maximal.

Background

Electron scattering experiments at large momentum transfer ($Q^2 \ge 1.5 \text{ GeV}^2$) and large Bjorken-x ($x_B = Q^2/2m\omega \ge 1.2$, where m is the nucleon mass and ω is the energy transfer) have found that short-range correlated nucleon pairs are predominantly proton-neutron pairs, are found in all nuclei, and account for almost all of the high-momentum nucleons (above the Fermi momentum) (1, 2).

On the theoretical side, significant progress has been made in describing SRC pairs from first principles. Many-body numerical calculations provide position and momentum space densities for a range of light to medium mass nuclei (12, 13), showcasing the universal nature of SRC pairs. Effective field theory techniques utilized scale separation and factorization to show that the dynamics of the nucleons within the pair is a short-distance phenomenon while pair formation is a long-range phenomenon sensitive to nuclear-structure details (14, 15).

Therefore, a comprehensive understanding of SRC pairs requires understanding pair-formation mechanisms, i.e., how SRC pairing changes with nuclear mass and neutron excess. Duer *et al.* (4), studied this by comparing proton and neutron knockout from a range of nuclei (12 C, 27 Al, 56 Fe, 208 Pb) with varying mass and neutron excess. They found an increased proton pairing probability in nuclei with a greater neutron excess. These extra high-momentum protons suggests that the excess neutrons in asymmetric nuclei form additional np SRC pairs.

However, since both mass and neutron excess increased together in the four measured nuclei, the data could not separate the contribution coming from the neutron excess from that of the increased

mass.

A previous inclusive-scattering measurement tried to address this by comparing ⁴⁰Ca and ⁴⁸Ca. Their results suggested a 17% increase in SRC pair formation due to the 40% increase in neutrons (*16*). However, a follow-up analysis found that due to the inclusive nature of the measurement, significant model-interpretation uncertainties are possible (*17*).

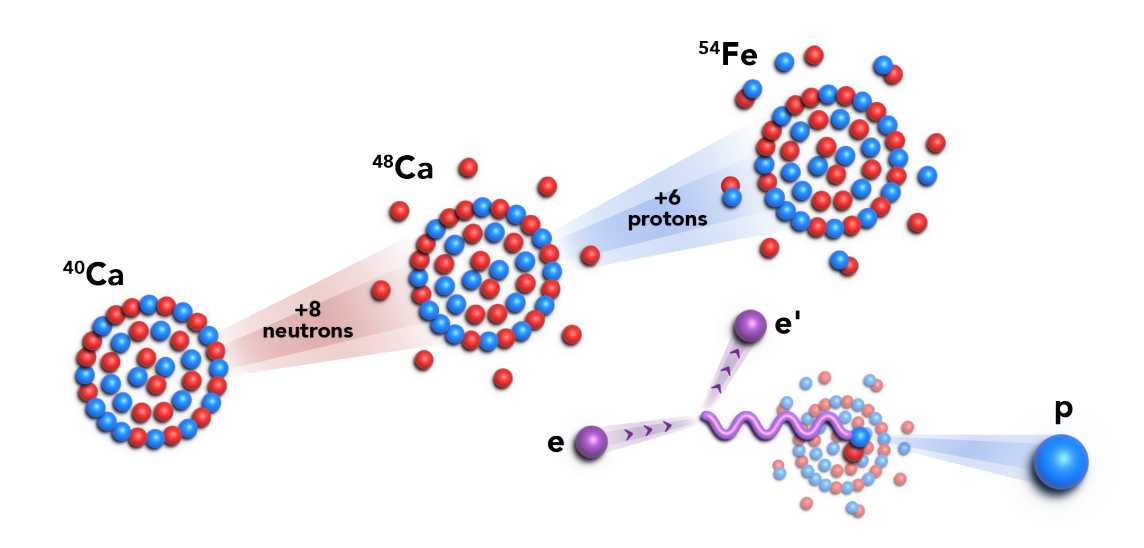


Figure 1: The "CaFe" nuclei showing the orbital structure of 40 Ca with 20 (blue) protons and 20 (red) neutrons in the 1s, 1p, and 2s, 1d orbitals, 48 Ca with eight more $1f_{7/2}$ neutrons, and 54 Fe with six more $1f_{7/2}$ protons. The lower right shows a schematic of the reaction, with an electron (purple) scattering from a nucleus by emitting a (purple) virtual photon which knocks out a proton (blue) from an np correlated pair in a nucleus.

To enhance the experimental sensitivity we also detected the proton knocked out from SRC pairs from ⁴⁰Ca and ⁴⁸Ca, and also measured ⁵⁴Fe for additional control of neutron excess versus nuclear mass effects, see Fig. 1.

Results

We measured the probability of proton knockout from SRC pairs by scattering 10.5-GeV electrons from ⁴⁰Ca, ⁴⁸Ca, and ⁵⁴Fe targets in Jefferson Lab's Hall C. The experiment, conducted in 2023, used the Super High Momentum Spectrometer (SHMS) (*18*) to detect scattered electrons at a central

scattering angle of $\theta_e = 8.3^{\circ}$ and a central momentum of 8.55 GeV/c, and the High Momentum Spectrometer (HMS) (19) to detect knocked-out protons at a central scattering angle of $\theta_p = 66.4^{\circ}$ and a central momentum of 1.325 GeV/c. These small-aperture magnetic spectrometers determine particle momentum by tracking curvature in the magnetic field. See Supplemental Material for details.

To select events dominated by proton knockout from SRC pairs, we required a squared momentum transfer $Q^2 \geq 1.8 \text{ GeV}^2$, Bjorken scaling variable $x \geq 1.2$, missing momentum $0.375 \leq p_{miss} \leq 0.700 \text{ GeV}/c$, and the angle between the recoil nucleus and the momentum transfer, $\theta_{rq} \leq 40^\circ$. These kinematic cuts isolate quasielastic scattering from high-initial-momentum nucleons, which are predominantly members of SRC pairs (8). They also reduce the effects of final state rescattering. The missing momentum, $p_{miss} = |\vec{p} - \vec{q}|$, corresponds approximately to the initial momentum of the struck nucleon and was calculated from the difference between the measured knocked-out proton momentum and the momentum transfer.

We extracted cross sections as a function of p_{miss} for each nucleus, integrated over the detector acceptances. From these, we computed cross-section ratios, which provide a relative measure of SRC-pair probabilities. Since the calculated momentum distributions of SRC pairs are almost identical in all nuclei, the ratios of 48 Ca to 40 Ca and 54 Fe to 48 Ca should be constant across the measured p_{miss} range. The constancy of our data with p_{miss} (Fig. 2) validates that we are measuring proton knockout from SRC pairs.

We then compared the averaged per-nucleus cross-section ratios (Fig. 3). We found that the SRC proton knockout ratio in 48 Ca is 1.10 ± 0.02 times that of 40 Ca. This is slightly lower than, though consistent within uncertainties, the measured inclusive ratio of 1.165 ± 0.014 (16). In contrast, the ratio of 54 Fe to 48 Ca is much larger, 1.49 ± 0.03 , indicating a substantially higher probability of SRC proton knockout in 54 Fe.

This pattern reveals a striking asymmetry. Increasing the neutron number by 40% from 40 Ca to 48 Ca leads to only a $\sim 10\%$ increase in SRC proton probability. However, adding six more protons from 48 Ca to 54 Fe results in a $\sim 50\%$ increase. These findings suggest that the eight $1f_{7/2}$ neutrons added in 48 Ca do not efficiently form SRC pairs with inner-orbital protons. In contrast, the added six $1f_{7/2}$ protons in 54 Fe pair strongly with the $1f_{7/2}$ neutrons, likely due to increased spatial overlap and favorable quantum numbers.

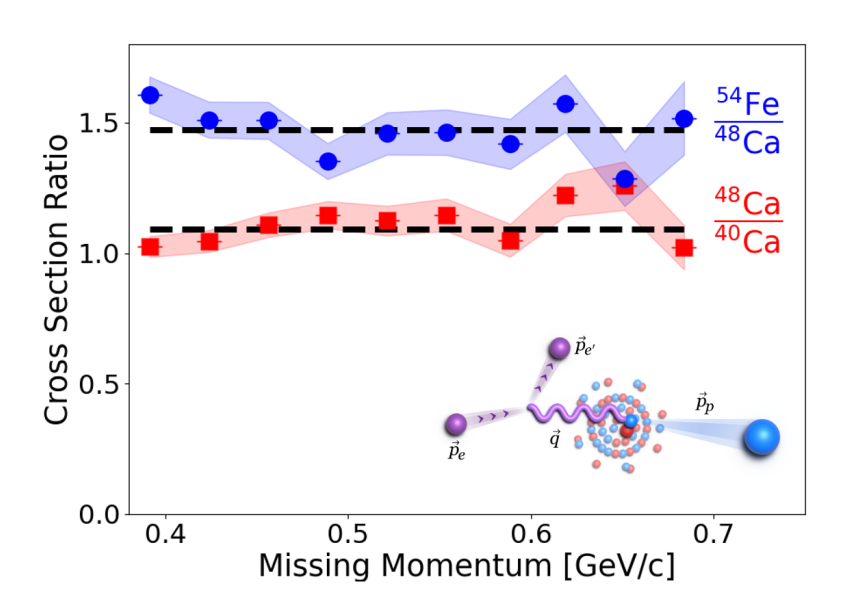


Figure 2: The per-nucleus (e, e'p) cross-section ratios for (red squares) 48 Ca/ 40 Ca and (blue circles) 54 Fe/ 48 Ca plotted versus missing momentum p_{miss} . The dashed lines show the weighted averages of data points. The corresponding χ^2/dof of the fits are 1.46 (48 Ca/ 40 Ca) and 1.32 (54 Fe/ 48 Ca). The inset shows the electron scattering from a nucleus, knocking out a proton from an SRC pair. The initial and scattered electron momenta are \vec{p}_e and $\vec{p}_{e'}$, the transferred momentum is \vec{q} and the outgoing proton momentum is \vec{p}_p . The missing momentum $p_{miss} = |\vec{p}_p - \vec{q}|$.

A schematic summary of the inferred intra- and inter-orbital pairing strengths is shown in the Fig. 3 inset. These results underscore the importance of orbital structure in driving SRC pair formation and provide new experimental constraints for models of dense nuclear matter.

We compared our results to different models (see Fig. 3). Colle *et al.* (21) employed a spatial approach using shell-model wave functions to calculate the number of *np* pairs at the same position using the Zero Range Approximation. This calculation previously reproduced the general trend of SRC pair probabilities from C to Pb.

Tropiano et al. (20) computed SRC-pair-sensitive momentum distributions using similarity renormalization group (SRG)-evolved operators and empirically tuned single-particle wave functions. The relative fractions of high-momentum protons should approximately equal the relative SRC-pair abundances. Both the spatial and momentum approaches slightly overestimated the ⁴⁸Ca/⁴⁰Ca ratio and dramatically underestimated the ⁵⁴Fe/⁴⁸Ca ratio.

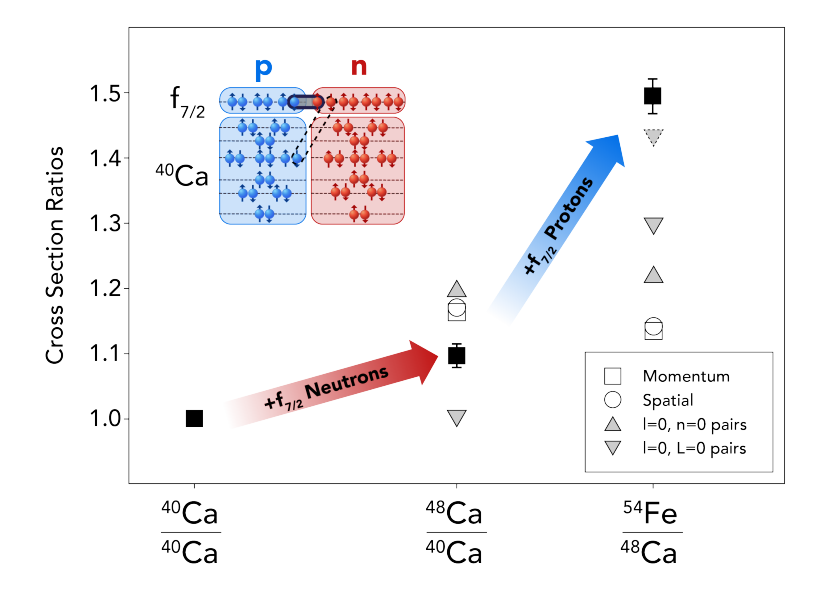


Figure 3: The per-nucleus integrated (e, e'p) cross-section ratios for 40 Ca/ 40 Ca, 48 Ca/ 40 Ca, and 54 Fe/ 48 Ca. The filled black squares show the data, the open squares show a momentum-distribution model (20), the open circles show the Zero Range Approximation spatial overlap model (21), the gray triangles show quantum pairing calculations of (upright triangles) the Colle (21) l=0, n=0 quantum-pairing model, and (inverted triangles) the more restrictive L=0, l=0 quantum-pairing model. The inverted triangle with the dashed-border has been corrected for rescattering of the outgoing protons. The upper-left inset shows the orbital structure of 40 Ca, the eight additional $1f_{7/2}$ neutrons in 48 Ca, and the six additional $1f_{7/2}$ protons in 54 Fe. The dashed ellipse represents the observed weak inter-orbital pairing and the solid ellipse represents the observed strong intra-orbital pairing.

Phenomenological models based on the orbital structure of nuclei offer additional guidance. Colle *et al.* (21) used shell-model wave functions to estimate the relative numbers of pp and pn pairs across nuclei. They found that allowing only nodeless (n = 0) S-state (l = 0) np pairs—better matched the previous data. This quantum selection rule overestimated our 48 Ca/ 40 Ca ratio and significantly underestimated the 54 Fe/ 48 Ca ratio.

We introduced a more selective quantum-pairing model, requiring SRC pairs to have both zero relative (l = 0) and total (L = 0) angular momentum (22). This eliminates pairing between nucleons in different orbitals and predicts: no increase in SRC pairs for ⁴⁸Ca relative to ⁴⁰Ca,

and a $\sim 30\%$ increase for 54 Fe due to the additional $1f_{7/2}$ protons. After accounting for different proton-rescattering effects from the different orbitals, the predicted 54 Fe/ 48 Ca SRC-pair ratio rises to 1.43. These results are within 10% of our experimental ratios.

Both of these quantum selection models neglect pp pairs, which should be at most a 10% effect in 54 Fe. In addition, our model neglects pairing between 1s neutrons and 2s protons (and vice versa), which should be about 10 times smaller than 1s - 1s and 2s - 2s pairing, due to the mismatch in the radial distribution.

Discussion

Our results point to a key organizing principle in the formation of SRC nucleon pairs: quantum number constraints imposed by shell structure are more important than either mass or neutron excess. Models based on spatial proximity or momentum distributions fail to describe the observed ratios. Instead, models that incorporate quantum-mechanical selection rules on the angular momentum states of pairing nucleons more accurately describe the data.

These findings impose important new constraints on theoretical models of nuclear structure and the dynamics of dense nuclear matter. They suggest that SRC-pair formation is not only simply a universal many-body feature of the nuclear wave function, but also reflects the quantum architecture of the nucleus itself. By demonstrating that angular momentum selection rules shape the SRC-pair landscape, this work opens new pathways for exploring the interplay between mean-field structure and short-range dynamics in nuclei.

These insights are important for modeling the structure of neutron-rich matter in extreme environments, including neutron stars, where SRC pairs influence the equation of state, neutrino opacities, and dense-matter response. Ultimately, bridging mean-field structure and short-range dynamics is key to a unified description of nuclear matter from finite nuclei to astrophysical scales.

References and Notes

- O. Hen, G. A. Miller, E. Piasetzky, L. B. Weinstein, Nucleon-Nucleon Correlations, Short-lived Excitations, and the Quarks Within. *Rev. Mod. Phys.* 89 (4), 045002 (2017), doi:10.1103/RevModPhys.89.045002.
- 2. E. I. Piasetzky, L. B. Weinstein, *Measurements of NN Correlations in Nuclei* (Springer Singapore), pp. 1–22 (2022), doi:10.1007/978-981-15-8818-1_60-1.
- 3. A. Schmidt, *et al.*, Probing the core of the strong nuclear interaction. *Nature* **578** (7796), 540–544 (2020), doi:10.1038/s41586-020-2021-6.
- 4. M. Duer, *et al.*, Probing high-momentum protons and neutrons in neutron-rich nuclei. *Nature* **560** (7720), 617–621 (2018), doi:10.1038/s41586-018-0400-z.
- 5. E. O. Cohen, *et al.*, Center of Mass Motion of Short-Range Correlated Nucleon Pairs studied via the A(e, e'pp) Reaction. *Phys. Rev. Lett.* **121** (9), 092501 (2018), doi:10.1103/PhysRevLett. 121.092501.
- 6. M. Duer, *et al.*, Direct Observation of Proton-Neutron Short-Range Correlation Dominance in Heavy Nuclei. *Phys. Rev. Lett.* **122**, 172502 (2019), doi:10.1103/PhysRevLett.122.172502.
- I. Korover, et al., 12C(e,e'pN) measurements of short range correlations in the tensor-to-scalar interaction transition region. Phys. Lett. B 820, 136523 (2021), doi:10.1016/j.physletb.2021. 136523.
- 8. I. Korover, *et al.*, Observation of large missing-momentum (e,e'p) cross-section scaling and the onset of correlated-pair dominance in nuclei. *Phys. Rev. C* **107** (6), L061301 (2023), doi:10.1103/PhysRevC.107.L061301.
- 9. R. Subedi, *et al.*, Probing Cold Dense Nuclear Matter. *Science* **320**, 1476–1478 (2008), doi: 10.1126/science.1156675.
- 10. B.-A. Li, B.-J. Cai, L.-W. Chen, J. Xu, Nucleon effective masses in neutron-rich matter. *Progress in Particle and Nuclear Physics* **99**, 29–119 (2018).

- 11. O. Hen, B.-A. Li, W.-J. Guo, L. B. Weinstein, E. Piasetzky, Symmetry energy of nucleonic matter with tensor correlations. *Phys. Rev. C* **91**, 025803 (2015), doi:10.1103/PhysRevC.91. 025803.
- 12. J. Carlson, S. Gandolfi, A. Gezerlis, Quantum Monte Carlo approaches to nuclear and atomic physics. *Prog. Theor. Exp. Phys.* **01A**, 209 (2012).
- 13. J. Carlson, *et al.*, Quantum Monte Carlo methods for nuclear physics. *Rev. Mod. Phys.* **87**, 1067 (2015), doi:10.1103/RevModPhys.87.1067.
- 14. R. Cruz-Torres, *et al.*, Many-Body Factorization and Position-Momentum Equivalence of Nuclear Short-Range Correlations. *Nature Physics* **17**, 306 (2020).
- 15. A. J. Tropiano, S. K. Bogner, R. J. Furnstahl, Short-range correlation physics at low renormalization group resolution. *Phys. Rev. C* **104** (3), 034311 (2021), doi:10.1103/PhysRevC.104. 034311.
- 16. D. Nguyen, *et al.*, Novel observation of isospin structure of short-range correlations in calcium isotopes. *Phys. Rev. C* **102**, 064004 (2020), doi:10.1103/PhysRevC.102.064004, https://link.aps.org/doi/10.1103/PhysRevC.102.064004.
- 17. R. Weiss, *et al.*, Extracting the number of short-range correlated nucleon pairs from inclusive electron scattering data. *Phys. Rev. C* **103** (3), L031301 (2021), doi:10.1103/PhysRevC.103. L031301.
- 18. S. Ali, *et al.*, The SHMS 11 GeV/c Spectrometer in Hall C at Jefferson Lab. *Nucl. Inst. and Meth. A* **under review** (2025).
- 19. O. K. Baker, *et al.*, The High Momentum Spectrometer drift chambers in Hall C at CEBAF. *Nucl. Instrum. Meth. A* **367**, 92–95 (1995), doi:10.1016/0168-9002(95)00737-7.
- 20. A. J. Tropiano, *et al.*, High-resolution momentum distributions from low-resolution wave functions. *Phys. Lett. B* **852**, 138591 (2024), doi:10.1016/j.physletb.2024.138591.

- 21. C. Colle, *et al.*, Extracting the mass dependence and quantum numbers of short-range correlated pairs from A(e, e'p) and A(e, e'pp) scattering. *Phys. Rev. C* **92**, 024604 (2015), doi:10.1103/ PhysRevC.92.024604.
- 22. A. Lane, *Nuclear Theory* (W.A. Benjamin, New York) (1964).
- 23. D. Bhetuwal, *et al.*, Constraints on the onset of color transparency from quasielastic C12(e,e'p) up to Q2=14.2(GeV/c)2. *Phys. Rev. C* **108** (2), 025203 (2023), doi:10.1103/PhysRevC.108. 025203.
- 24. M. Sargsian, Private communication.
- 25. C. Yero, *et al.*, Probing the Deuteron at Very Large Internal Momenta. *Phys. Rev. Lett.* **125** (26), 262501 (2020), doi:10.1103/PhysRevLett.125.262501.
- 26. D. Dutta, K. Hafidi, M. Strikman, Color Transparency: past, present and future. *Prog. Part. Nucl. Phys.* **69**, 1–27 (2013), doi:10.1016/j.ppnp.2012.11.001.
- 27. O. Hen, *et al.*, Momentum sharing in imbalanced Fermi systems. *Science* **346**, 614–617 (2014), doi:10.1126/science.1256785.
- 28. M. Duer, *et al.*, Measurement of Nuclear Transparency Ratios for Protons and Neutrons. *Phys. Lett.* **B797**, 134792 (2019), doi:10.1016/j.physletb.2019.07.039.
- 29. O. Benhar, A. Fabrocini, S. Fantoni, I. Sick, Spectral function of finite nuclei and scattering of GeV electrons. *Nuclear Physics A* **579** (3), 493–517 (1994), doi:https://doi.org/10.1016/0375-9474(94)90920-2, https://www.sciencedirect.com/science/article/pii/0375947494909202.

Acknowledgments

We acknowledge the efforts of the staff of the Accelerator and Physics Divisions at Jefferson Lab that made this experiment possible. We acknowledge support from the National Science Foundation MPS-Ascend Postdoctoral Research Fellowship Grant No. 2137604, the U.S. Department of Energy, the Jefferson Lab Nathan Isgur Fellowship, and the United States-Israel Binational Science

Foundation (BSF) grant 2018093. Jefferson Science Associates operates the Thomas Jefferson National Accelerator Facility for the DOE, Office of Science, Office of Nuclear Physics under contract DE-AC05-06OR23177. We are also grateful to all granting agencies providing funding support to the authors of this project.

Supplementary materials

Materials and Methods

Supplementary Text

Tables S1 to S2

Figures S1 to S6

References (7-29)

Supplementary Materials for

Quantum Number Constraints from Shell Structure Govern Short-range Nucleon Pairing

D. Nguyen[†], C. Yero[†], H. Szumila-Vance, F. Hauenstein, N. Swan, L.B. Weinstein*, J. Kahlbow, G.A. Miller, A. Schmidt, E. Piasetzky, O. Hen, C. Ayerbe Gayoso, E. Cohen, P. Datta, A. Denniston, B.R. Devkota, M. Diefenthaler, C. Fogler, B.R. Gamage, D. Higinbotham, I. Korover, C. Morean, M. Nycz, M. Satnik, S. Seeds, P. Sharp, M. Suresh, A.S. Tadepalli, R. Wagner, E. W. Wertz

*Corresponding author. Email: weinstein@odu.edu

†These authors contributed equally to this work.

This PDF file includes:

Materials and Methods Supplementary Text Tables S1 to S2 Figures S1 to S6

Materials and Methods

Table S1: Target information

Target	Areal Thickness	Purity
	(g/cm ²)	
⁴⁰ Ca	0.800	100%
⁴⁸ Ca	1.050	90%
⁵⁴ Fe	0.415	98%

The measurement described in this paper was carried out in 2022-2023 using the facilities of Hall C of the Thomas Jefferson National Accelerator Facility (Jefferson Lab) in Newport News, Virginia, see Fig. S1. We scattered a 30–60 μ A, 10.5-GeV electron beam from 40 Ca, 48 Ca, and 54 Fe targets, see Table S1. We detected the scattered electrons in the SHMS spectrometer (23), which has a nominal solid angle of ≈ 4.0 msr with a fractional momentum acceptance of $-10\% \le \frac{\Delta p}{p_0} \le 22\%$. We used a pair of horizontal drift chambers for tracking, two pairs of x-y scintillator hodoscope planes for triggering and timing, and a lead-glass calorimeter for electron identification. The SHMS was set to a central momentum $p_0 = 8.55$ GeV/c, a central angle of $\theta_e = 8.3^\circ$, and thus with a broad range of momentum transfers centered on $Q^2 = 1.97$ GeV².

We detected the knocked-out protons in the HMS spectrometer (23), which has a nominal solid angle of 6 msr and an $\pm 9\%$ fractional momentum acceptance. We used a pair of horizontal drift chambers for tracking, and two pairs of x-y scintillator hodoscope planes for triggering and timing. The HMS central momentum was $p_0 = 1.325$ GeV/c and the central angle was $\theta_p = 66.4^\circ$ for data taking. The missing momentum and energy are $\vec{p}_{miss} = \vec{p}_p - \vec{q}$ and $E_{miss} = \omega - T_p$ where \vec{p}_p and T_p are the three-momentum and kinetic energy of the detected proton, respectively.

We traced the electron and the proton back to the interaction vertex and determined their time difference. Out-of-time events were used to estimate and subtract the random coincidence background from the coincidence peak.

We measured elastic electron scattering from hydrogen, H(e, e') and H(e, e'p), for calibrations and normalization. We calibrated the momentum of the SHMS by varying the magnetic field to vary p_0 and thus scan the location of the hydrogen elastic peak across the SHMS focal plane. We

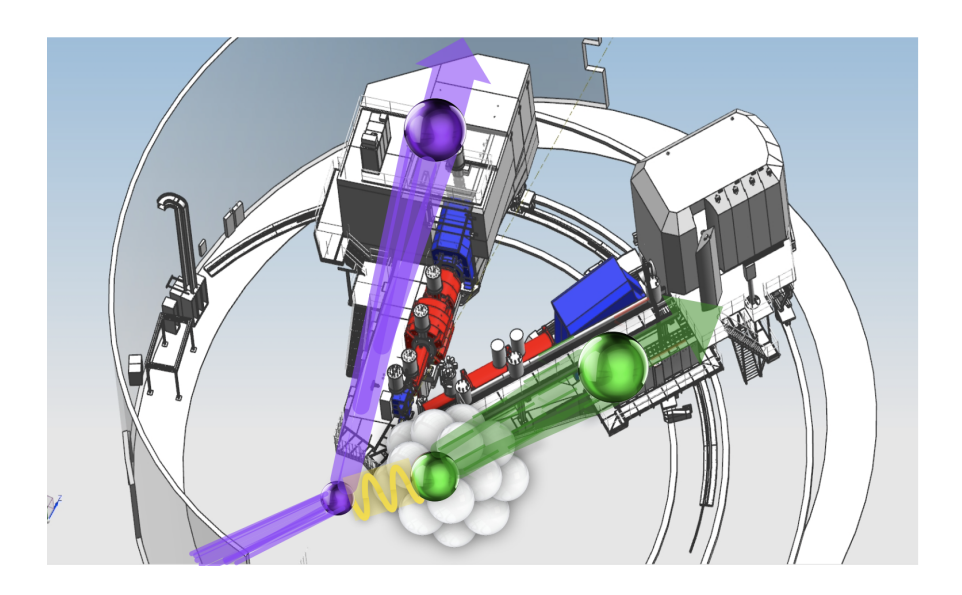


Figure S1: Hall C spectrometers: The SHMS (left) detected the scattered electron (purple) and the HMS (right) detected the knocked-out proton (green).

determined the overall normalization and checked that the spectrometers were performing well by comparing the measured H(e,e') and H(e,e'p) cross sections to the world data. This normalization agreed to better than 5%. The effects of this normalization (e.g., any spectrometer inefficiencies) cancel in the cross-section ratios. We determined the tracking efficiency in each spectrometer by selecting events with good particle hits in the central parts of the scintillator hodoscopes and determining the fraction of events with good tracks in the drift chambers. Electronic deadtime correction factors were measured in each spectrometer with a dedicated random trigger.

Table S2: Cross section Ratio

Tubic DE. Closs section Italio							
Ratio	Data	Momentum	Spatial	l=0, n=0	l=0, L=0		
48 <u>Ca</u> 40 <u>Ca</u>	1.10±0.02	1.164	1.170	1.200	1.000		
⁵⁴ Fe ⁴⁸ Ca	1.49±0.03	1.136	1.140	1.222	1.300		

Both Ca targets were stored in light mineral oil (typically $(CH_2)_n$) to prevent oxidation. The targets had a thin film of oil when installed in the scattering chamber, which subsequently evaporated with time and beam heating. We measured the target oil contamination in two ways. First, we measured the H(e, e'p) peak at $E_{miss} = 0$ and $p_{miss} = 0$ for the Ca-target (e, e'p) calibration runs to directly measure the H contamination. Second, we used the rate of SHMS single-arm

electron triggers per incident electron for Ca(e,e') to measure the total target thickness (Ca plus oil contamination) in each run. The ⁴⁸Ca oil contamination decreased exponentially from about 3% to about 0.5% during the data taking as the oil evaporated in the vacuum of the target chamber. The ⁴⁰Ca oil contamination was constant at about 0.5%. These total oil contamination values were consistent with the measured H contamination for $(CH_2)_n$ mineral oil. We subtracted the oil contamination run-by-run using our measured C(e,e'p) data, scaled to the estimated carbon content of the oil.

We also used the measured 40 Ca data to subtract the 10% 40 Ca contribution to our 90%-pure 48 Ca target data. We did not correct the 54 Fe data for the 2% 56 Fe contamination.

To select events with protons from SRC pairs we required that all events have momentum transfer $Q^2 \ge 1.8 \text{ GeV}^2$, $x \ge 1.2$ and $0.375 \le p_{miss} \le 0.700 \text{ GeV/c}$. The Q^2 and x cuts select quasielastic scattering events, where the electron scatters elastically from a single bound nucleon. The $p_{miss} = 0.375 \text{ GeV/c}$ lower limit corresponds approximately to the onset of NN SRC-pair dominance (8).

The outgoing proton can rescatter in the residual nucleus (final state interactions or FSI), shifting p_{miss} to larger values and contaminating the SRC-pair sample. Most of these collisions deflect the outgoing proton slightly, leading to a peak at $\theta_{rq} \approx 70^{\circ}$, where θ_{rq} is the angle between the recoil momentum $\vec{p}_r = -\vec{p}_{miss} = \vec{q} - \vec{p}_p$ and the three-momentum transfer \vec{q} (24). This same effect can be seen in proton knockout from deuterium (25). We therefore required $\theta_{rq} \leq 40^{\circ}$ for the SRC-pair events to reduce the effects of FSI.

We calculated the depletion of the outgoing protons due to rescattering out of our experimental acceptance (26) using a Glauber calculation (27) and calculated the uncertainty by comparing these transparency ratios with those from a Glauber calculation with different parameters and using $T \propto A^{-0.289}$ (28). The transparency factor ratios used were $T_{48/40} = 0.910 \pm 0.013$ and $T_{54/48} = 0.967 \pm 0.013$.

For each target nucleus A we converted the number of detected events to a cross section:

$$\sigma = \frac{N}{Qt \epsilon T_A R_A}$$

where N is the number of events for nucleus A, Q is the integrated number of incident electrons, t is the areal target thickness in nuclei/cm² calculated from Table S1, $\epsilon = \epsilon_{HMS}^T \epsilon_{SHMS}^T \epsilon_{LT} \epsilon_{EDT} \epsilon_{HMS}^p$

is an efficiency correction that includes the HMS and SHMS tracking efficiencies, the electronic dead time, the computer live time, and the HMS proton detection efficiency, T_A is the nuclear transparency for nucleus A, and R_A is the radiative correction factor.

 R_A is determined from the ratio of the radiated to unradiated plane-wave impulse approximation cross sections calculated using the spectral function developed by O. Benhar (29) for 12 C, 56 Fe, and 197 Au and the Hall C "SIMC" event generator and spectrometer simulator integrated over our experimental kinematics. Because R_A varied very slowly from C to Au ($R_C = 0.741$, $R_{Fe} = 0.734$, $R_{Au} = 0.603$), we used the same radiative correction factor for 40 Ca, 48 Ca, and 54 Fe, and assigned a systematic uncertainty in the ratio of 1%.

We integrated the number of events over the experimental acceptances for each nucleus and calculated the 48 Ca to 40 Ca and 54 Fe to 48 Ca ratios.

The systematic uncertainties include contributions from radiative and transparency corrections, and from cut variations. For each cut, we determined the 1σ "reasonable" cut variation. We then varied all the cuts simultaneously, randomly selecting the value of each cut from a gaussian distribution and calculating the cross section ratios for each set of cuts. The uncertainty in the cross section ratio is the standard deviation of the resulting ratio distribution. The cut variation uncertainties were 1% for both the 48 Ca/ 40 Ca and the 54 Fe/ 48 Ca ratios. Due to taking ratios of similar nuclei, the systematic uncertainties in the ratios were small.

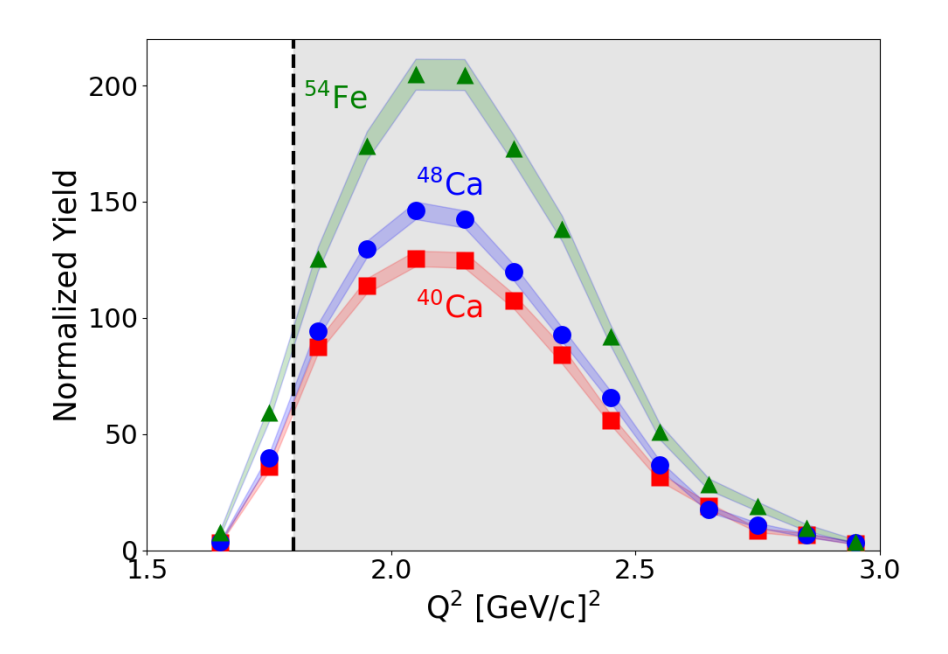


Figure S2: The normalized yield plotted versus Q^2 for 40 Ca, 48 Ca, and 54 Fe. The red squares show the 40 Ca, the blue circles show the 48 Ca, and The green triangles show the 54 Fe data. We excluded data to the left of the dashed line at $Q^2 = 1.8$ (GeV/c)².

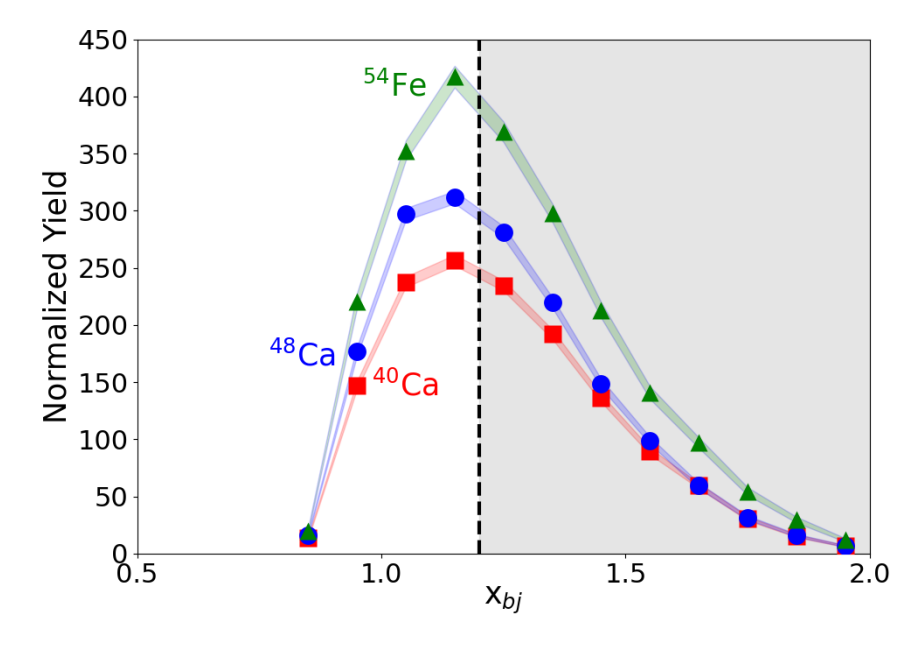


Figure S3: The normalized yield plotted versus x_{bj} for 40 Ca, 48 Ca, and 54 Fe. The red squares show the 40 Ca, the blue circles show the 48 Ca, and The green triangles show the 54 Fe data. We excluded data to the left of the dashed line at $x_{bj} = 1.2$.

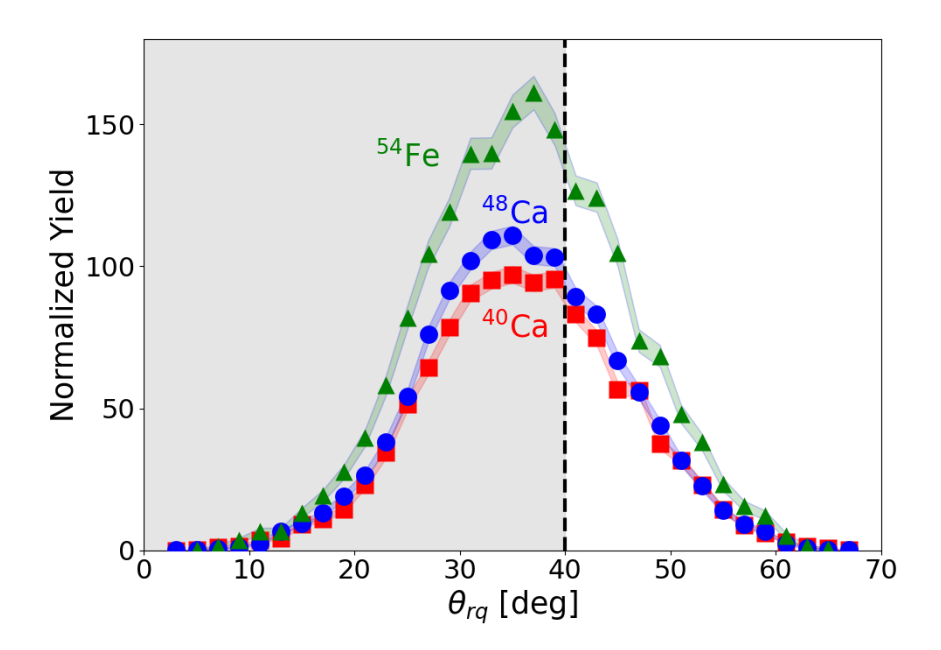


Figure S4: The normalized yield plotted versus θ_{rq} for 40 Ca, 48 Ca, and 54 Fe. The red squares show the 40 Ca, the blue circles show the 48 Ca, and The green triangles show the 54 Fe data. We excluded data to the right of the dashed line at $\theta_{rq} = 40$ deg.

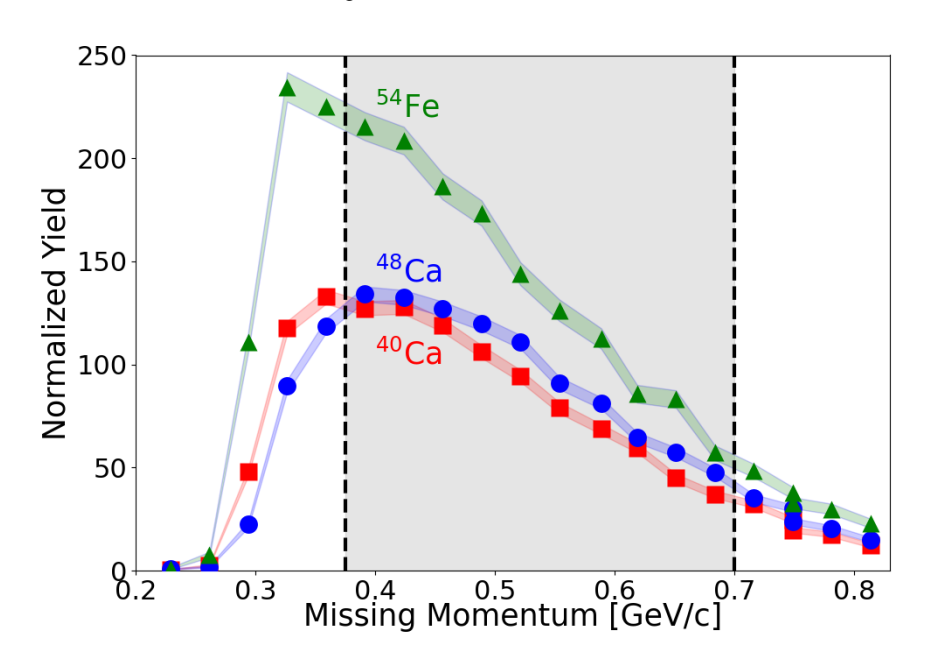


Figure S5: The normalized yield plotted versus p_{miss} for 40 Ca, 48 Ca, and 54 Fe. The red squares show the 40 Ca, the blue circles show the 48 Ca, and The green triangles show the 54 Fe data. We excluded data outside the The dashed lines at $p_{miss} = 0.375$ GeV and $p_{miss} = 0.7$ GeV.

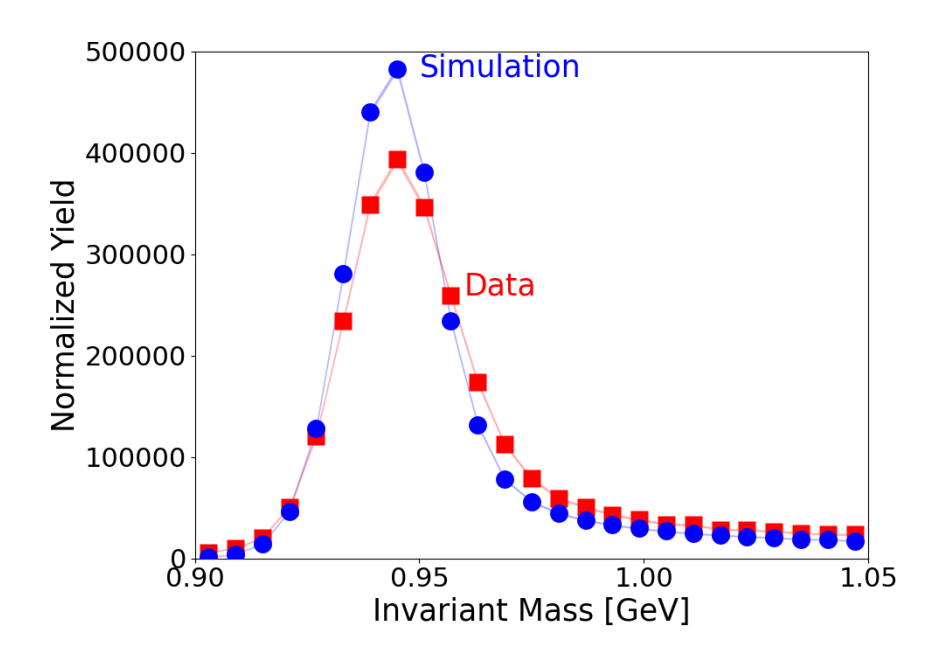


Figure S6: The normalized yield for the invariant mass, The red squares show the 2D data and the blue circles show a 2D simulation for H(e, e'p).

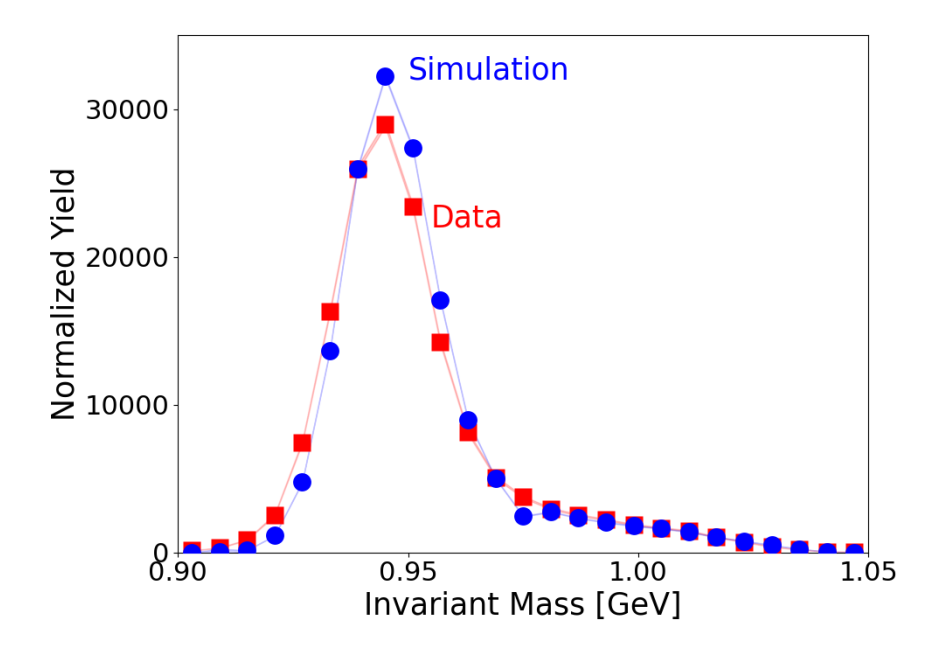


Figure S7: The H(e, e') normalized yield plotted versus invariant mass, for data (req squares) and simulation (blue circles) using a parametrization of the world H(e, e') data.